PNAS RESEARCH ARTICLE | BIOPHYSICS AND COMPUTATIONAL BIOLOGY

Phenol-soluble modulins PSMα3 and PSMβ2 form nanotubes that are cross-α amyloids

Mark A. B. Kreutzberger[a,1], Shengyuan Wang[b,1], Leticia C. Beltran[a], Abraham Tuachi[b], Xiaobing Zuo[c], Edward H. Egelman[a,2], and Vincent P. Conticello[b,d,2]

Contributed by Edward H. Egelman; received November 28, 2021; accepted April 8, 2022; reviewed by Meytal Landau and Louise Serpell

Phenol-soluble modulins (PSMs) are peptide-based virulence factors that play significant roles in the pathogenesis of staphylococcal strains in community-associated and hospital-associated infections. In addition to cytotoxicity, PSMs display the propensity to self-assemble into fibrillar species, which may be mediated through the formation of amphipathic conformations. Here, we analyze the self-assembly behavior of two PSMs, PSMα3 and PSMβ2, which are derived from peptides expressed by methicillin-resistant *Staphylococcus aureus* (MRSA), a significant human pathogen. In both cases, we observed the formation of a mixture of self-assembled species including twisted filaments, helical ribbons, and nanotubes, which can reversibly interconvert in vitro. Cryo–electron microscopy structural analysis of three PSM nanotubes, two derived from PSMα3 and one from PSMβ2, revealed that the assemblies displayed remarkably similar structures based on lateral association of cross-α amyloid protofilaments. The amphipathic helical conformations of PSMα3 and PSMβ2 enforced a bilayer arrangement within the protofilaments that defined the structures of the respective PSMα3 and PSMβ2 nanotubes. We demonstrate that, similar to amyloids based on cross-β protofilaments, cross-α amyloids derived from these PSMs display polymorphism, not only in terms of the global morphology (e.g., twisted filament, helical ribbon, and nanotube) but also with respect to the number of protofilaments within a given peptide assembly. These results suggest that the folding landscape of PSM derivatives may be more complex than originally anticipated and that the assemblies are able to sample a wide range of supramolecular structural space.

cross-α amyloid | bacterial pathogenesis | peptide nanotube | cryo-EM

Significance

The formation of cross-α amyloids has been shown by crystallographic analysis of the highly cytolytic peptide PSMα3, a secreted virulence factor associated with the human pathogen *Staphylococcus aureus*. However, the relationship of the crystallographic cross-α structure to self-assembled filaments of PSMα3 and its relevance to other phenol-soluble modulin (PSM) peptides remained an open question. We report the cryo–electron microscopy structural analysis of three nanotubes derived from self-assembly of PSMα3 and PSMβ2 peptides in aqueous solution. In each case, the nanotubes are derived from self-association of cross-α amyloid protofilaments. The self-assembly behavior of *S. aureus* PSMα3 and PSMβ2 peptides provides strong evidence for the importance of the cross-α fold in self-assembled peptide and protein structures in general and for PSMs in particular.

Methicillin-resistant *Staphylococcus aureus* (MRSA) (1, 2) is a leading human pathogen that contributes significantly to morbidity and mortality in community-associated and hospital-associated staphylococcal infections (3, 4). The severity of *S. aureus* infections has been correlated with the expression of virulence factors, the most important of which are a family of secreted peptides known as the phenol-soluble modulins (PSMs) (5, 6). The PSMs, thus named for their ability to partition into a phenol-rich phase through extraction (7, 8), fall into two distinct classes that can be distinguished on the basis of peptide length. The PSMα class is typically 20 to 25 amino acids in length, while the PSMβ class is nearly twice as long at ∼44 to 45 amino acids. PSMs display multiple activities that are associated with *S. aureus* pathogenesis, including cytolysis (8), immunomodulation (9), antimicrobial activity (10), structuring of biofilms, and dissemination of biofilm-associated pathogens (11).

A critical structural feature that relates the different classes of PSMs is the presence of sequence amphipathicity (5), as exemplified for *S. aureus* PSMα3 and PSMβ2 (Fig. 1 *A*–*C*). NMR structural analyses of PSMα3 (Protein Data Bank [PDB]: 5KGY) and PSMβ2 (PDB: 5KGZ) in trifluoroethanol (TFE)-water mixtures indicated the formation of amphipathic helical structures for the isolated peptides in solution (12) (Fig. 1 *D* and *E*). The resultant amphipathic character of the PSM peptides has been proposed to be a strong determinant of the cytolytic membrane activity that is associated with MRSA pathogenesis (13, 14). Sequence amphipathicity can also drive self-assembly behavior (15–17). In particular, sequences that adopt conformations that segregate polar and nonpolar residues to different faces often undergo self-association into filamentous structures that is mediated through hydrophobic interactions. These observations have led to the suggestion that a functional reciprocity may exist between membrane-active peptides (e.g., antimicrobial peptides) and self-assembled peptide filaments (e.g., amyloids) (18–20). Structural investigations of the *S. aureus* PSMs in aqueous solution provided evidence for the formation of filamentous assemblies (21–25), which led to the suggestion that PSMs behave as functional bacterial amyloids (21). However, the relationship of this self-assembly behavior to the cytolytic

Author contributions: E.H.E. and V.P.C. designed research; M.A.B.K., S.W., L.C.B., A.T., X.Z., E.H.E., and V.P.C. performed research; M.A.B.K., L.C.B., E.H.E., and V.P.C. analyzed data; and M.A.B.K., E.H.E., and V.P.C. wrote the paper.

Reviewers: M.L., Technion - Israel Institute of Technology; and L.S., University of Sussex.

The authors declare no competing interest.

[1]M.A.B.K. and S.W. contributed equally to this work.

[2]To whom correspondence may be addressed. Email: egelman@virginia.edu or vcontic@emory.edu.

This article contains supporting information online at http://www.pnas.org/lookup/suppl/doi:10.1073/pnas.2121586119/-/DCSupplemental.

Published May 9, 2022.

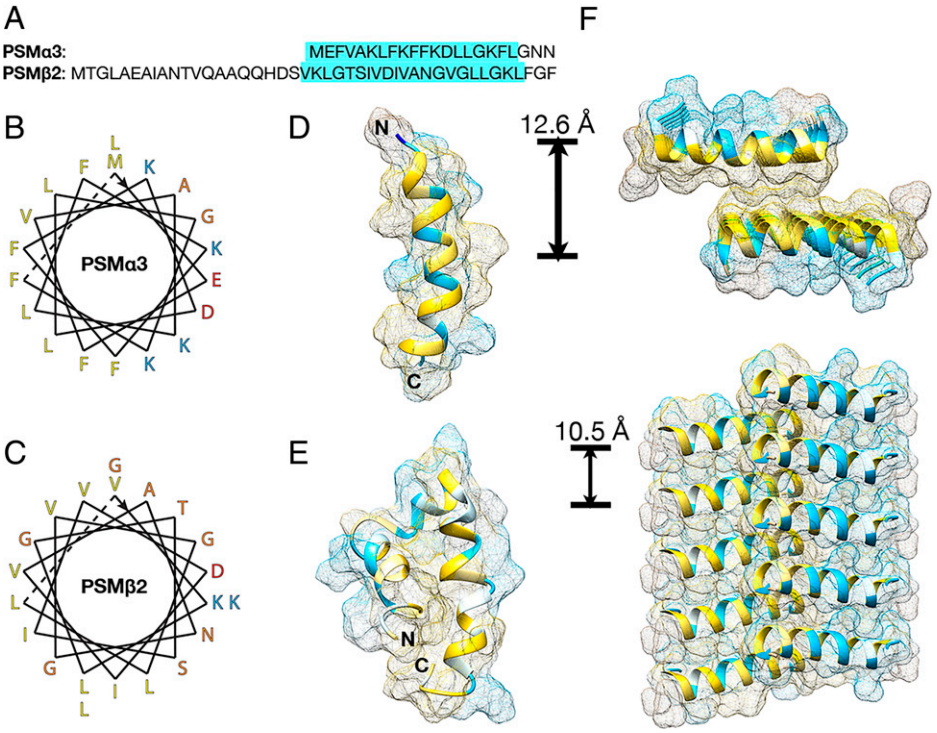

Fig. 1. Macromolecular structure of PSMs PSMα3 and PSMβ2. (*A*) Sequences of *S. aureus* peptides PSMα3 and PSMβ2. Amphipathic helices are highlighted in cyan. (*B* and *C*) Helical wheel diagrams corresponding to the amphipathic helices of PSMα3 (*B*) and PSMβ2 (*C*). (Amino acid color code: yellow, hydrophobic; blue, basic; red, acidic; orange, polar). (*D*) Solution NMR structure of PSMα3 (PDB ID: 5KGY). (*E*) Solution NMR structure of PSMβ2 (PDB ID: 5KGZ). (*F*) Top (*Upper*) and side (*Lower*) views of a bilayer sheet in cross-α array in the crystal structure of PSMα3 (PDB ID: 5I55). The coloring in the ribbon diagrams is derived from the Kyte-Doolittle hydrophobicity scale in which cyan corresponds to polar residues, white corresponds to neutral residues, and yellow corresponds to hydrophobic residues.

properties of PSMs and, more generally, to *S. aureus* pathogenesis has been hotly debated (21, 23, 26, 27).

Due to its high level of cytotoxicity and up-regulated expression in pathogenic MRSA strains (8), the self-assembly behavior of PSMα3 has been extensively investigated. In a landmark structural investigation, Landau and coworkers (22) determined the crystal structural of PSMα3 (PDB: 5I55), which revealed the presence of a cross-α helical assembly (Fig. 1*F*). The amphipathic helices are stacked within the crystal structure of PSMα3 such that their axes are oriented perpendicular to the stacking direction, which results in the formation of a hydrophobic interface between structurally adjacent helical stacks. The resultant bilayer structure resembles the hydrophobic mating interfaces between β-strands that are observed in cross-β structures derived from crystallographic analysis of amyloidogenic oligopeptides (28). The amphipathic helices of PSMα3 are arranged in an antiparallel orientation across the mating interface, which, in the wild-type (WT) peptide, results in a lateral offset between facially opposed protomers.

Subsequent crystallographic analyses of site-directed alanine mutants (27) and a racemic (D/L) pair of PSMα3 peptides (29) have confirmed that the cross-α structure is conserved with minor sequence-specific structural alterations. In the crystal structures of two PSMα3 mutants, K12A (PDB: 6GQ2) and G16A (PDB: 6GQC), the amphipathic helices are directly opposite across the bilayer interface, which provided evidence that packing polymorphism can occur in the cross-α fold with respect to the WT structure (27). X-ray fiber diffraction analysis of oriented bundles of PSMα3 filaments (22, 27), derived from in vitro self-assembly of the synthetic peptide, displayed periodicities at 10.5 Å and 12 Å that were similar to the axial helix stacking and lateral sheet lamination distances, respectively, that were observed in crystallographic analysis of PSMα3. These reflections were oriented nearly orthogonal to each other in the corresponding diffraction pattern, with the sheet stacking distance observed along the meridian, as would be expected for cross-α structural arrangement in which the stacked helices were aligned nearly parallel to the long axis of the filament. In addition, previously published negative-stain transmission electron microscopy (TEM) images of the corresponding assemblies revealed the presence of a variety of filamentous species (22, 27, 29), including wide ribbons and/or tubes. The observation of such structural polymorphism is common among cross-β assemblies (30–33) and often results from differences in peptide packing at the hydrophobic interfaces within and between protofilaments.

Here, we report the cryo–electron microscopy (cryo-EM) structural analysis of nanotubes derived from self-assembly of PSMα3 and PSMβ2 peptides in aqueous solution. We provide evidence that the polymorphic structures of the nanotubes arise from self-association of cross-α helical protofilaments in which the amphipathic helices pack in a bilayer arrangement to form the inner and outer walls of the respective nanotubes. The occurrence of structural polymorphism has been reported as a consequence of self-assembly of amphipathic molecules in vitro in which variations in initial conditions can profoundly influence the morphological distribution of the resultant assemblies (34).

Results

In order to gain insight into the influence of sequence amphipathicity on self-assembly within the PSM peptides, structural analyses of synthetic peptides (*SI Appendix*, Figs. S1 and S2) derived from *S. aureus* PSMα3 and PSMβ2 were undertaken under conditions that promoted self-assembly in vitro. The corresponding peptides, each representative of a different class of PSMs, show a degree of structural similarity in that the presence of a long

amphipathic helix was predicted from sequence analysis and subsequently confirmed by NMR structural determination in TFE/water mixtures (Fig. 1) (12–14). The PSMβ peptides are distinguished from the PSMα peptides by the presence of an N-terminal sequence extension, which, in the solution NMR structure of *S. aureus* PSMβ2, folds in association with the C-terminal amphipathic helix to form a three-helix bundle structure (Fig. 1*E*) (12). However, the NMR structures of PSMα3 and PSMβ2 peptides are unlikely to be fully representative of the structure in aqueous solution, in which both peptides display a strong tendency toward self-association into higher-order assemblies.

To investigate the structure of the PSMα3 nanotubes and determine their relationship to the cross-α protein fold, the assembly conditions for PSMα3 were varied over a range of pH and temperature in order to obtain more homogeneous specimens. At near-neutral pH (7 to 8) and ambient temperature, TEM imaging revealed the presence of a mixture of assemblies, in which flexible, twisted filaments with varying degrees of bundling and/or lateral association dominated the population (Fig. 2*A* and *SI Appendix*, Fig. S3), as reported in earlier studies (22, 27, 29). Thermal annealing of the sample above ambient temperature altered the morphological distribution such that it favored formation of high aspect ratio tubular assemblies (*SI Appendix*, Fig. S4). Initially, solutions of the PSMα3 peptide were heated to 90 °C followed by slow cooling to ambient temperature, which resulted in the formation of wide diameter tubes (apparent width ∼1,000 to 1,600 Å) that were stable at ambient temperature but polymorphic in lateral dimensions. Incubation of aqueous solutions of PSMα3 (380 μM) at the physiological temperature of 37 °C for 72 h in [tris(hydroxymethyl)methylamino]propanesulfonic acid (TAPS) buffer (10 mM, pH 8) resulted in the conversion of the twisted filaments to nanotubes of different width with the average value centered at ∼600 Å (*SI Appendix*, Fig. S5). Notably, incubation of these nanotubes at ambient temperature for 72 h caused reversion to the twisted filaments, which could then be converted back to tubes through incubation at 37 °C. These results suggested that self-assembly of the nanotubes was a dynamic process that could be reproducibly controlled through variations in assembly conditions, particularly temperature, as has been observed previously for nanotubes derived from designed peptides (34).

The high degree of variability in nanotube morphology and the reversibility of nanotube assembly prompted a search for preparative conditions in which tube formation was better controlled and more reproducible. Under acidic conditions, negative-stain TEM analysis revealed the presence of an apparently uniform population (measured width of ∼600 Å) of PSMα3 nanotubes after 24 h of incubation of an aqueous solution of peptide (300 μM, pH 2) at ambient temperature. The resultant nanotubes persisted without reversion or decomposition over a period of weeks. At earlier stages in the assembly process, twisted filaments, helical ribbons, and nanotubes were observed to coexist in the reaction mixture (*SI Appendix*, Fig. S6). However, the self-assembly process appeared to converge on the formation of nanotubes as the incubation time increased over a period of 24 h. TEM was employed to monitor the structural progression over time. Twisted filaments were initially observed that coalesced into helical ribbons (Fig. 2*B*). The latter assemblies gradually closed to form the PSMα3 nanotubes, presumably through sealing of the edges of the helical ribbons, as observed earlier for cross-β nanotubes (35–40). However, twisted filaments were occasionally observed to emerge from the ends of the nanotubes (Fig. 2*C*), which argued that they served a critical role as components of the internal structure of the nanotubes. Twisted filaments and helical ribbons have been postulated as on-pathway intermediates (33, 41) in the self-assembly of nanotubes from peptides

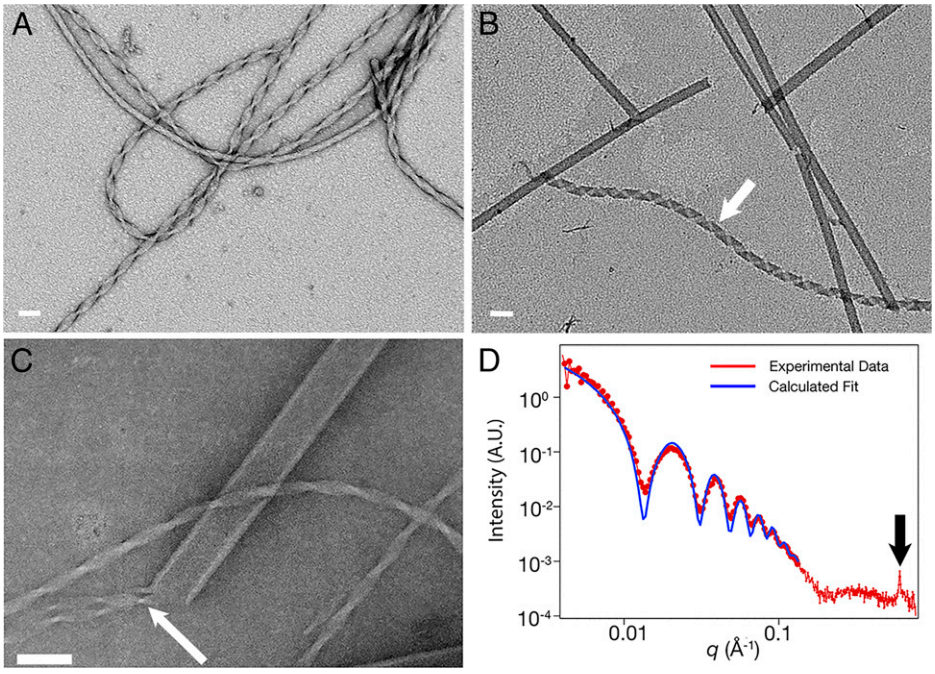

Fig. 2. Structural analysis of PSMα3 assemblies. (*A*) Negative-stain TEM image of twisted filaments of PSMα3 (380 μM) assembled in TAPS buffer (10 mM, pH 8.0). (Scale bar, 50 nm.) (*B*) Positive-stain TEM image of helical ribbons (white arrow) and nanotubes of PSMα3 (300 μM) assembled from under acidic conditions (pH 2) after 1-h incubation. (Scale bar, 100 nm.) (*C*) Darkfield STEM image of unstained PSMα3 (300 μM) at pH 2, in which twisted filaments are observed to emerge from the ends of the nanotubes (white arrow). (Scale bar, 50 nm.) (*D*) Comparison of the experimental synchrotron SAXS scattering curve for a mature solution of PSMα3 (300 μM) nanotubes at pH 2 to the calculated fit to a hollow cylinder form factor. The black arrow indicates the presence of a Bragg peak at a q value of 0.61 Å^{-1} (d = 10.3 Å), which corresponds to the helical stacking distance within the solvated nanotubes. A.U., arbitrary units.

(35–40) and proteins (42, 43) and in the formation of tubular supramolecular assemblies from other chiral monomers (44–49).

As observed under all conditions within the pH range 6 to 8, the circular dichroism (CD) spectra of the PSMα3 peptides at pH 2 were consistent with the adoption of an α-helical conformation within the assemblies (*SI Appendix*, Fig. S7), as noted in previous investigations (14, 22). Synchrotron small-angle X-ray scattering (SAXS)/wide-angle X-ray scattering (WAXS) analysis of a mature population of nanotubes resulted in a series of well-defined oscillations of intensity on the momentum transfer (q), which was consistent with formation of thin-walled, wide-diameter hollow cylinders (Fig. 2*D*). Analysis of the SAXS data yielded a low-resolution model of a nanotube having an ∼30-Å thick annular shell with an inner radius of 164 ± 8 Å. In addition, a Bragg diffraction peak was observed at a q value of 0.61 $Å^{-1}$ (d = 10.3 Å), which corresponded closely to the axial stacking distance of 10.5 Å observed between helices in the crystal structure of PSMα3 (PDB: 5I55) (22). SAXS analysis was previously employed to infer the formation of an apparently uniform population of cross-β nanotubes of similar dimensions (diameter of 52 nm) derived from self-assembly of the amyloidogenic peptide Aβ (16–22), which occurred through an analogous process under acidic conditions (35).

While these results suggested that the formation of PSMα3 nanotubes resulted from the self-association of cross-α amyloid filaments, cryo-EM analysis was undertaken in order to gain insight into the structure of the assemblies at near-atomic resolution. Initial cryo-EM imaging of what was previously assumed (based upon negative stain TEM and SAXS) to be a homogeneous nanotube preparation indicated the presence of several distinct populations of nanotubes that differed in apparent diameter (Fig. 3*A*). These results provided evidence that negative-stain TEM and SAXS measurements, while useful tools for the structural analysis of assemblies, are insufficient to distinguish heterogeneity that arises from the presence of closely related structural polymorphs. Since such polymorphism is common in self-assembled filaments (50), claims of homogeneity based on limited resolution methods of structural analysis should be treated with skepticism until confirmed with near-atomic resolution analysis.

Two distinct populations of the PSMα3 nanotubes, with diameters of ∼370 Å versus ∼410 Å, were analyzed using iterative helical real-space reconstruction (IHRSR) (51, 52) from the corresponding cryo-EM images after two-dimensional (2D) classification (Fig. 3*A*). The diameter of ∼600 Å observed for the negatively stained sample can be simply explained by the flattening that can frequently occur due to both dehydration and strong adsorption to a grid (53). For example, a 370-Å diameter tube that was completely flattened would have a measured width of 580 Å, while a 410-Å tube would be flattened to a width of 644 Å. Atomic models were built into the three-dimensional (3D) volumes after determination of the helical

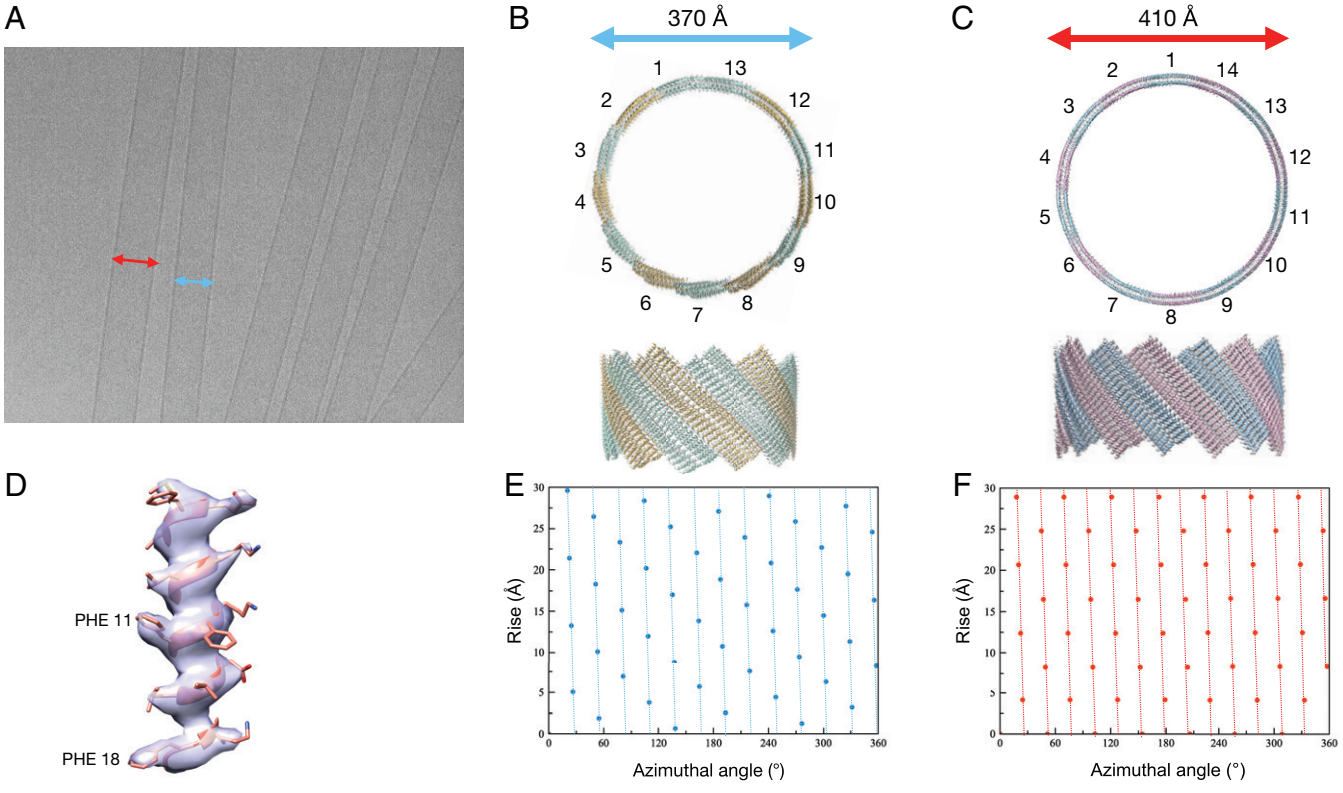

Fig. 3. Cryo-EM structure of the PSMα3 nanotubes. (*A*) Cryo-electron micrograph of PSMα3 nanotubes of different diameters, the two most common diameters being near 370 Å (blue double arrow) and 410 Å (red double arrow). (*B*) Model of the smaller diameter tube fit into its density map (light gray). The top image shows a view through the lumen of the tube, while the bottom image shows a side view. The protofilaments are distinguished by alternating gold and green strands. (*C*) Model of the larger diameter tube fit into its density map (light gray). Top and bottom images are the same views as in *B*. The protofilaments are indicated as alternating pink and blue strands. (*D*) Model of a single PSMα3 peptide fit into its corresponding density map. (*E*) Helical net of the smaller PSMα3 dimeter tubes. The convention used is that the surface of the tube is unrolled and is being viewed from the outside surface of the nanotube. The positions of the blue dots correspond to the helical arrangement of the asymmetric units. These smaller diameter tubes are generated from 13 protofilaments with a left-handed twist (light blue lines) in the absence of rotational point group symmetry (C_1 symmetry). Each asymmetric unit is related to an adjacent one in the same protofilament by a rise of 8.2 Å and rotation of −2.1°. (*F*) Helical net of the larger diameter PSMα3 tubes. The asymmetric units are indicated by the red dots. This larger diameter tube has C_7 rotational point group symmetry with 14 left-handed protofilaments (red lines). Adjacent asymmetric units in each protofilament are related by a rise of 8.3 Å and rotation of −2.2°.

symmetry (Fig. 3 *B* and *C*), which generated reconstructions at resolutions (map versus model) of 3.9 Å and 4.1 Å for the smaller and larger diameter tubes, respectively. Consistent with such resolution estimates, side chain density could easily be seen (Fig. 3*D*). The smaller diameter tubes, which corresponded to the larger population within the sample, had C_1 symmetry and contained 13 cross-α protofilaments (Fig. 3*E*). In comparison, the larger diameter tubes had C_7 symmetry and consisted of 14 cross-α protofilaments. The tetrameric asymmetric units within the two assemblies were structurally related and were derived from self-association of the facially amphipathic PSMα3 peptides in an antiparallel orientation at the inner–outer interface of the bilayer nanotube (*vide infra*). We estimated that the difference in stability between nanotubes based on 13 versus 14 protofilaments was unlikely to be large due to the small difference in interior angles between protofilaments within the cross-sections of the respective nanotubes. If the diameter of the larger nanotube, ∼410 Å, was scaled by a factor of (13/14), that is, the ratio of the number of protofilaments between the smaller and larger diameter nanotubes, the resultant diameter for the smaller nanotube would be 380 Å, close to the measured diameter of ∼370 Å from cryo-EM analysis. These results provided an explanation for the observation that the nanotube diameters appeared to cluster about discrete values, which presumably corresponded to different numbers of protofilaments within the assembly. We hypothesize that the population distribution of nanotubes, as judged by the observed diameter and the corresponding number of protofilaments in a nanotube cross-section, depended strongly upon preparative conditions (e.g., pH and temperature), as has been observed for other biological and designed helical filaments (34, 54–58).

The packing of the α-helical peptides within the PSMα3 crystal structure (Fig. 4*A*) was observed to be quite similar to the corresponding helix packing in the PSMα3 nanotube structures (Fig. 4 *B* and *C*). In both the 13- and 14-protofilament nanotubes, the supramolecular structure was derived from self-association of protofilaments based on stacked pairs of PSMα3 peptides (Fig. 4 *G* and *H*). The helices in the crystal structure form an amphipathic bilayer with a helix–helix distance of 12.6 Å across the interface (*SI Appendix*, Fig. S8*A*) (22). The protofilaments within the PSMα3 nanotubes retain this bilayer architecture (*SI Appendix*, Fig. S8 *B* and *C*); however, the packing of the nanotube bilayers is more symmetrical across the bilayer interface in that the helices are nearly in register rather than offset. The stacking axis of the cross-α helices in the crystal structure was aligned along the crystallographic b-axis (Fig. 4*D*), whereas the helix stacking axes of the cross-α protofilaments for each PSMα3 nanotube were tilted with respect to the helical axis (Fig. 4 *E* and *F*), allowing for the assembly of either 13 or 14 of these strands into the tubes (Fig. 3 *B* and *C*). The asymmetric unit of the smaller diameter tubes (Fig. 4 *B* and *G*)

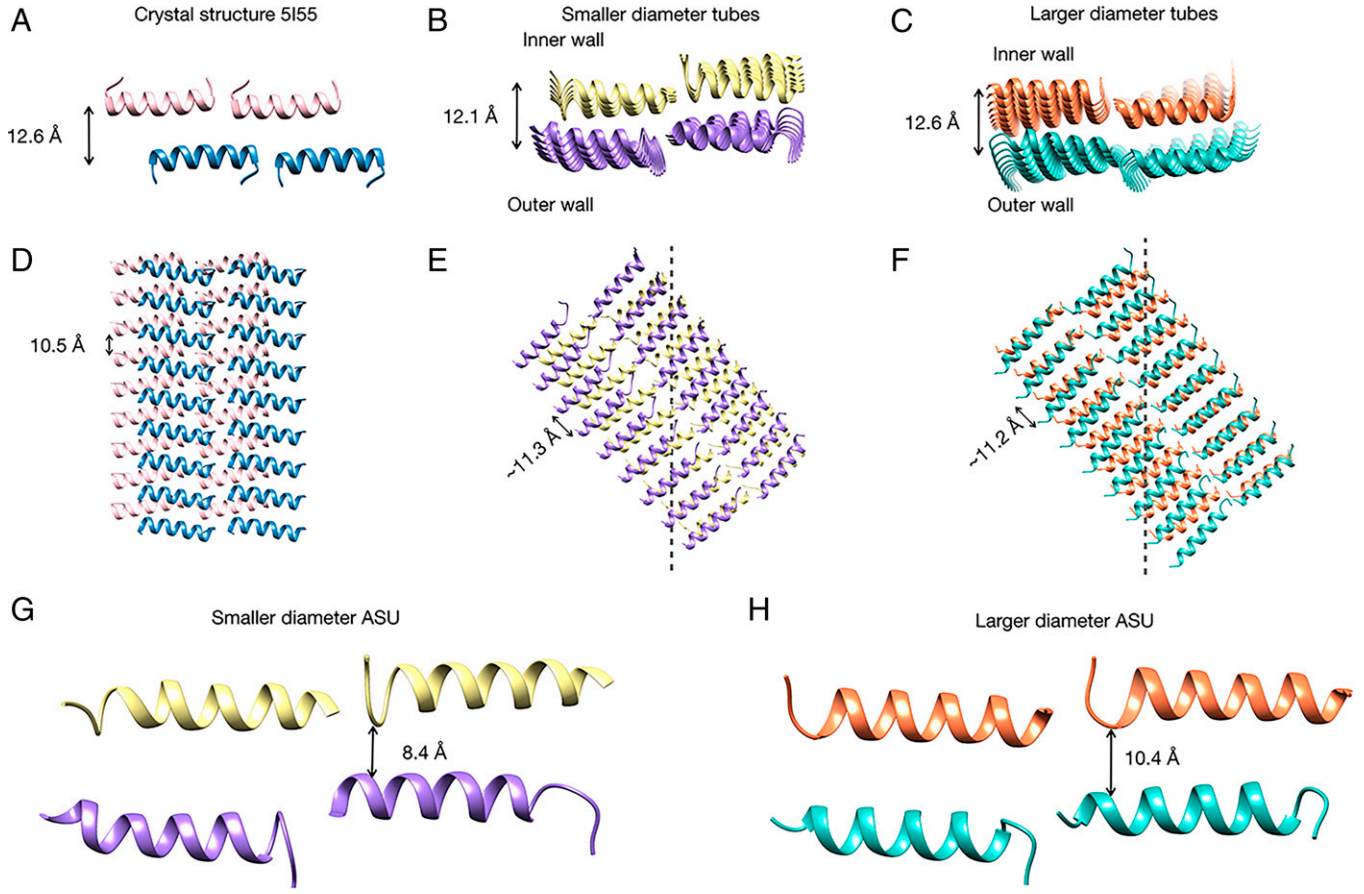

Fig. 4. Comparison of the organization of cross-α strands of PSMα3 in the crystal structure and nanotubes. (*A*) Helix packing of the PSMα3 strands in the crystal structure of the WT *S. aureus* peptide (PDB 5I55). (*B*) Packing of α-helices within a protofilament cross-section in the smaller diameter PSMα3 nanotube. (*C*) Packing of α-helices within a protofilament cross-section in the larger diameter PSMα3 nanotube. (*D*) Side view of the cross-α strand of the PSMα3 crystal structure. (*E*) Side view of a protofilament strand of the smaller diameter PSMα3 nanotube. The gray dashed line indicates the helical axis of the nanotube. (*F*) Side view of a protofilament strand of the larger diameter PSMα3 nanotube. The gray dashed line indicates the helical axis of the nanotube. (*G*) Asymmetric unit (ASU) of the smaller diameter PSMα3 tubes indicating the closest approach of helices across the inner–outer interface of the bilayer. (*H*) Asymmetric unit of the larger diameter PSMα3 tubes indicating the closest approach of helices across the inner–outer interface of the bilayer.

displayed a shorter distance between the inner and outer helices across the bilayer interface within the asymmetric unit than was observed for the larger diameter tubes (Fig. 4 *C* and *H*). Despite this difference in distance across the inner–outer packing interface, the arrangement of PSMα3 helices within the asymmetric units of protofilaments derived from the smaller and larger tubes was quite similar. The helix stacking distance of 11.2 to 11.3 Å, observed in the outer wall protofilaments of both the smaller and larger nanotubes, was slightly greater than the corresponding distance of 10.5 Å in the crystal structure of the WT PSMα3 peptide (Fig. 4 *D*–*F*). As observed previously in the crystal structures of PSMα3 mutants (27), differences in the interfacial interactions between helices could account for packing polymorphism that resulted in the observed differences between stacking distances.

While the hydrophobic interfaces within the cryo-EM structures and the crystal structure of PSMα3 were similar with respect to the orientation of helices in the asymmetric unit, differences were observed in side-chain packing that might be attributed to the formation of protofilaments versus crystals. Within protofilaments of the smaller and larger nanotubes, the positions of the Met1 residues on the inner wall of the nanotube protofilaments (*SI Appendix*, Fig. S9 *A* and *B*) were deeply buried in the hydrophobic space between the inner and outer walls. In contrast, Met1 (more exactly, selenomethionine 1) in the crystal structure faced away from the bilayer interface (*SI Appendix*, Fig. S9*C*). Furthermore, the orientation of the helix backbone in the asymmetric unit of the nanotube protofilaments appeared to also change the positioning of Glu2, which was displaced toward the tube center and was in close proximity to adjacent peptide helices (*SI Appendix*, Fig. S9 *D* and *E*), possibly forming critical structural interactions between helices in the asymmetric unit. The placement of Glu2 in the crystal structure was at an intermediate position in comparison to its arrangement within the two nanotubes (*SI Appendix*, Fig. S9*F*). Given the lower resolution of the cryo-EM structures compared to the crystal structure, the exact position of Glu2 was difficult to determine with certainty. However, because the nanotubes are formed at pH values that would protonate glutamate residues, the structural role of the Glu2 residue on nanotube formation posed an interesting question, particularly as it resided at interfaces within and between protofilaments that mediated lateral association.

In contrast to PSMα3, the PSMβ derivatives from *S. aureus* have been less well characterized. Prior TEM analyses have demonstrated that the PSMβ1 and PSMβ2 peptides assemble into filaments in aqueous buffer (23, 25). CD spectropolarimetry and Fourier transform infrared spectroscopy provided evidence for the presence of β-sheets within the corresponding assemblies. However, the solution NMR structure of PSMβ2 in water/TFE mixtures was observed to be a three-helix bundle structure (Fig. 1*E*) (12). In our hands, the *S. aureus* PSMβ2 peptide could be solubilized in aqueous buffers at concentrations less than 600 μM within a wide pH range (5–10) at ambient temperature. Under these conditions, the corresponding CD spectra were consistent with a predominantly α-helical conformation (*SI Appendix*, Fig. S10). Negative-stain TEM analysis indicated the presence of a variety of self-assembled species displaying different morphological features, in which the population distribution depended on the buffer pH (*SI Appendix*, Fig. S11). At neutral to basic pH values of 7 to 10, PSMβ2 displayed a preference for tubular morphologies (apparent width of ∼450 Å) over filaments and helically coiled ribbons. However, conditions that favored a homogeneous population of nanotubes could not be identified, which precluded an effective SAXS analysis of the assemblies.

Despite the heterogeneous population distribution of the peptide specimen, cryo-EM was employed to structurally analyze the nanotubes that resulted from self-assembly of PSMβ2 (560 μM) in *N*-cyclohexyl-3-aminopropanesulfonic acid buffer (10 mM, pH 10.0) (Fig. 5*A*). 2D classification of a morphologically similar subset of nanotubes afforded a population of uniform diameter (∼310 Å) that served as the basis of further structural analysis. IHRSR (51, 52) was employed for helical reconstruction of the corresponding 3D volume at 4.3-Å resolution in which side chain density could be visualized and into which an atomic model could be built (Fig. 5 *B* and *C*). Similar to the PSMα3 nanotubes, the PSMβ2 tubes were based on a helical arrangement of asymmetric units containing four peptides. The PSMβ2 nanotubes had C_6 symmetry and contained 12 protofilaments. The 12-protofilament arrangement gives rise to the pattern of cross-hatching seen in negatively stained scanning transmission electron microscopy (STEM) images of PSMβ2 nanotubes (*SI Appendix*, Fig. S12).

The internal structure of the respective protofilaments was based on a bilayer arrangement of peptides in which the asymmetric unit was arranged such that two peptides defined the outer and inner surface of the nanotube. As observed for the PSMα3 nanotubes, a hydrophobic surface representation of the bilayer interface within the PSMβ2 protofilaments (*SI Appendix*, Fig. S8*D*) indicated that the hydrophobic faces of the amphipathic helices were buried at the inner–outer interfaces off the protofilaments. In contrast to the NMR structure of PSMβ2 in solution (Fig. 1*E*), the PSMβ2 peptides within the assembly corresponded to a helix-turn-helix motif rather than a three-helix bundle (Fig. 5 *D* and *E*). The anisotropy of the helical hairpin structure promoted stacking of the subunits in a cross-α arrangement that would be otherwise precluded in the globular three-helix fold. Notably, the computational algorithm RoseTTAFold (59) predicted a structural model from the sequence of PSMβ2 that closely resembled that observed for the individual subunits in the atomic model of the PSMβ2 nanotube (*SI Appendix*, Fig. S13). The cross-α arrangement of helical hairpins within the PSMβ2 nanotubes differed from the cryo-EM structures of two recently reported nanotubes that resulted from self-assembly of designed helical hairpin motifs (60). In the latter case, the individual peptide helices were preferentially oriented nearly parallel to the helical axis of the assembly, rather than in a plane perpendicular to it, as was observed for the PSMβ2 nanotubes.

Discussion

Despite differences in peptide sequence and length, PSMα3 and PSMβ2 self-assembled into remarkably similar nanotubes based on the recently reported cross-α amyloid structural paradigm (22). All three nanotubes were derived from lateral association of cross-α protofilaments that resulted from axial stacking of helices within the asymmetric unit (*SI Appendix*, Fig. S14). In each case, the asymmetric unit consisted of a tetramer of the respective peptides. Because each PSMα3 peptide contains one α-helix while each PSMβ2 peptide contains two α-helices, the asymmetric units of the corresponding nanotubes consisted of four and eight helices, respectively. The packing arrangement of helices within the protofilament defined the exterior and interior surfaces of the corresponding nanotubes. While the helical symmetries of the nanotubes differed, in each case the protofilaments were oriented similarly within the respective nanotubes, that is, along left-handed 12-start (PSMβ2 tubes),

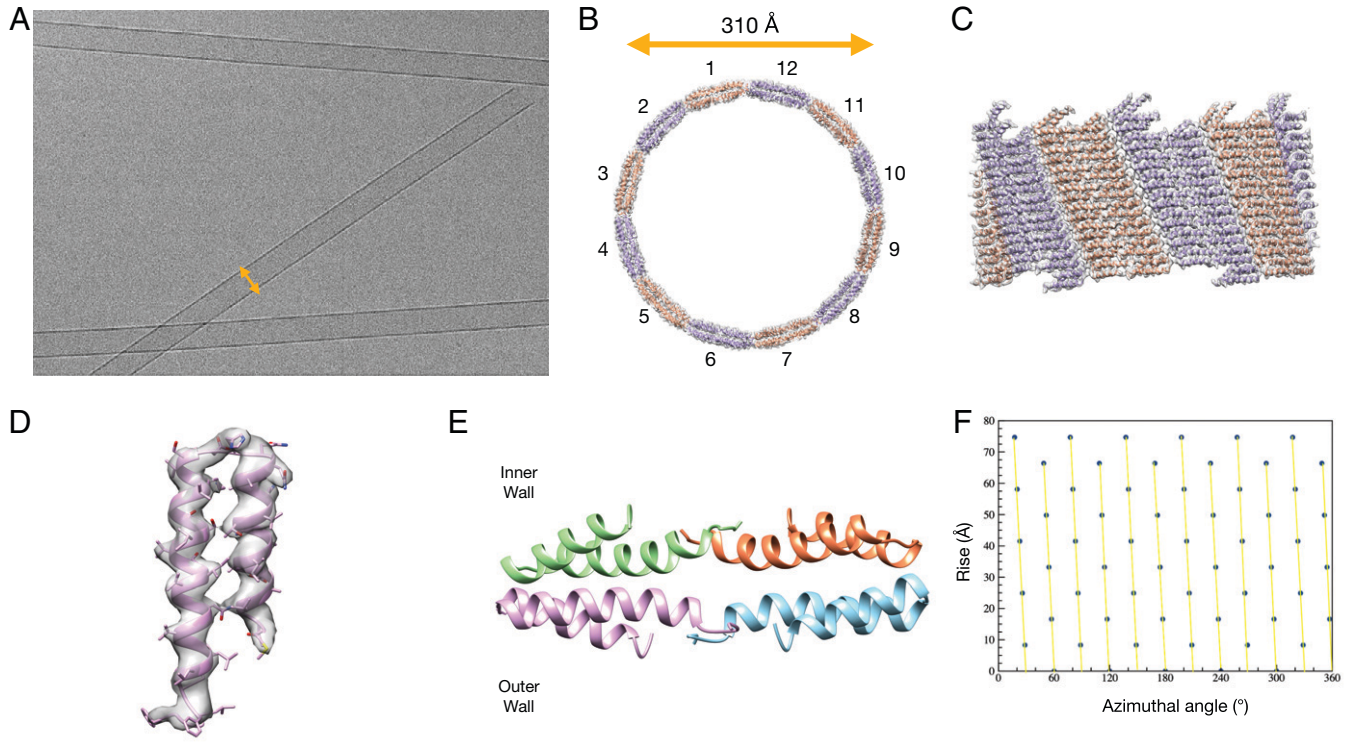

Fig. 5. Cryo-EM structure of the PSMβ2 nanotubes. (*A*) Cryo-electron micrograph of the PSMβ2 nanotubes. The orange double arrow indicates a 310-Å diameter. (*B*) Top view of the PSMβ2 nanotube model fit into its density map (light gray). (*C*) Side view of the PSMβ2 nanotube model fit into the density map. Protofilaments are colored in alternating orange and purple. (*D*) Single PSMβ2 peptide model fit into its corresponding density map. (*E*) Asymmetric unit of the PSMβ2 nanotubes. The asymmetric unit consists of four peptides with eight helices. (*F*) Helical net of the PSMβ2 nanotube. The asymmetric units are depicted as blue dots, and the yellow lines indicate the presence of the 12 left-handed protofilaments in the structure.

13-start (smaller PSMα3 tubes), and 14-start (larger PSMα3 tubes) helices (Figs. 3 *E* and *F* and 5*F*). The left-handed arrangement of cross-α protofilaments in PSMα3 and PSMβ2 nanotubes contrasted with the right-handed orientation of cross-α protofilaments in a series of designed nanotubes based on coiled-coil motifs (61–63).

Protein Interfaces, Surfaces, and Assemblies analysis (64) of the respective nanotube structures indicated that significant surface area was buried at the axial helix stacking interfaces between asymmetric units within a protofilament for the smaller diameter PSMα3 nanotubes (~2,100 Å^2), the larger diameter PSMα3 nanotubes (~1,900 Å^2), and the PSMβ2 nanotubes (~2,600 Å^2). These interactions corresponded to the interfaces between layers of helices in structurally adjacent asymmetric units along the respective 12-, 13-, and 14-start lines, as described above and depicted in the helical net diagrams (Figs. 3 *E* and *F* and 5*F*). In contrast, the contact across the lateral interfaces between protofilaments was less extensive, with substantially less surface area buried per laterally adjacent asymmetric units for the PSMα3 (~290 Å^2 and ~260 Å^2) and PSMβ2 (~280 Å^2) nanotubes. This can be seen in our comparison of the interfaces between protofilaments across all three nanotube structures (*SI Appendix*, Fig. S14). A similar situation was observed in a series of designed cross-*a* nanotubes (61–63), in which the buried surface area between α-helical subunits within a protofilament was far more extensive than that of the lateral interface between helices in adjacent protofilaments. Computational analysis of the latter nanotubes provided evidence that the robust axial stacking interfaces within a protofilament were natively designable, while the weaker lateral interaction between protofilaments represented natively rare structural interfaces (63). Despite the locally weak lateral interface, the presence of multiple structural interactions along the contour length of the cross-α protofilaments presumably provided the driving force for lateral association into nanotubes. We propose that a similar phenomenon underlies the self-association of PSMα3 and PSMβ2 protofilaments into nanotubes. The frequent observation in EM images of protofilaments emerging from the open ends of the nanotubes (e.g., Fig. 2*C* and *SI Appendix*, Fig. S6*A*) provided additional data in support of this hypothesis.

The interactions between adjacent protofilaments were also quite different between PSMα3 and PSMβ2. For both PSMα3 nanotubes, the lateral interactions between protofilaments had mostly hydrophobic contacts (*SI Appendix*, Fig. S14 *B* and *D*), resulting in a near continuation of the bilayer between protofilaments. For PSMβ2, the bilayer-like nature was only present within single protofilaments (*SI Appendix*, Fig. S14*F*), and contacts between adjacent protofilaments were likely mediated by interactions between interfacial histidine residues as well as possible histidine–asparagine interactions (*SI Appendix*, Fig. S15).

Despite this structural similarity in supramolecular architecture between the two classes of PSM nanotubes, the PSMα3 and PSMβ2 assemblies differed in the manner in which the helices were oriented at the inner–outer interface within the asymmetric units (Fig. 6 *A* and *B*). The PSMα3 peptides were oriented in an antiparallel arrangement while the PSMβ2 peptides were oriented in parallel. In addition, the PSMα3 and PSMβ2 nanotubes differed in the way in which the asymmetric units oriented themselves within the protofilaments in order to accommodate the formation of bilayer nanotubes. For the PSMα3 assemblies, the helices within the protofilaments were nearly in register across the inner–outer interface of the nanotube (Fig. 4 *B* and *C*). This local arrangement necessitated that the protofilaments develop a pronounced tilt, ~45°, with respect to the helical axis

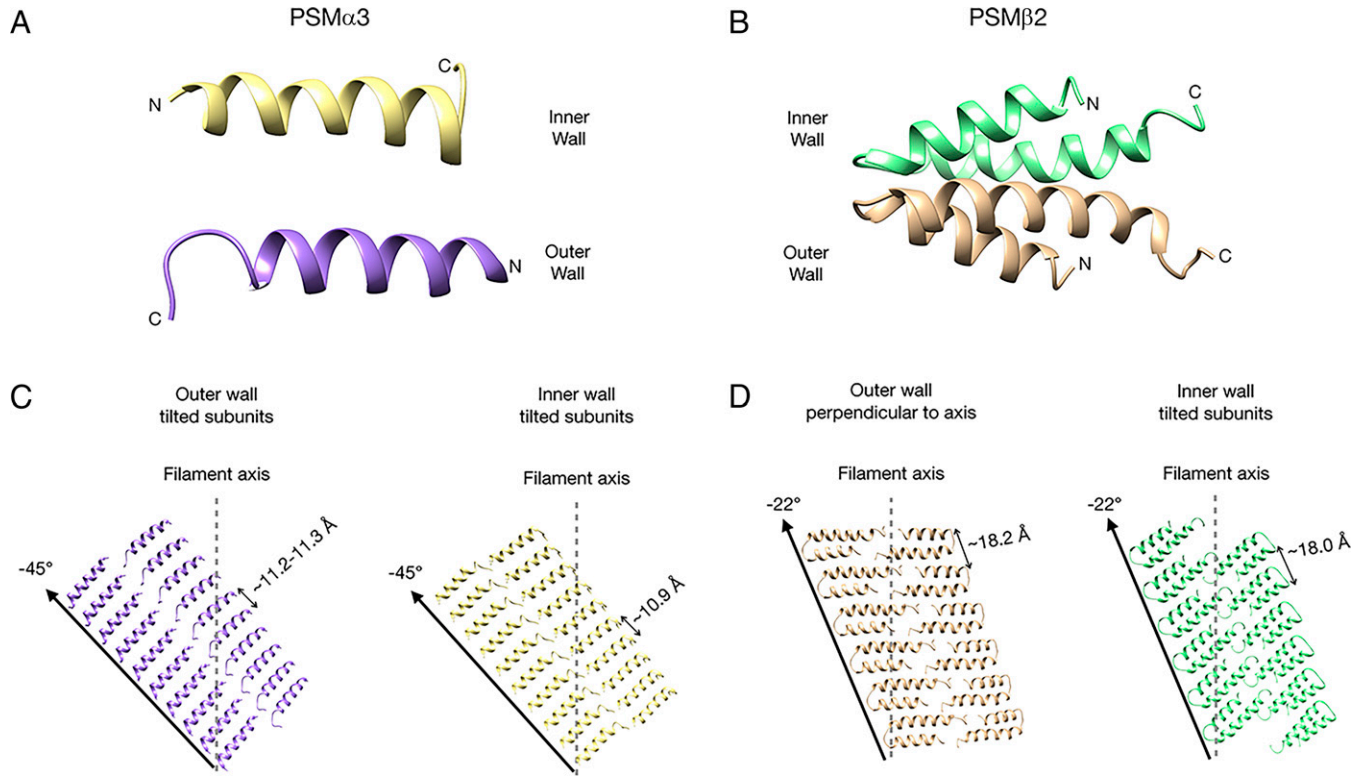

Fig. 6. Comparison of PSMα3 and PSMβ2 nanotube protofilaments. (*A*) PSMα3 subunits on the inner and outer walls are arranged antiparallel to each other. (*B*) PSMβ2 subunits on the inner and outer walls are arranged parallel to each other. (*C*) The tilt of the PSMα3 cross-α protofilaments with respect to the filament's helical axis is −45°. The orientations of inner and outer wall subunits are the same. (*D*) The tilt of the PSMβ2 protofilaments with respect to the filament axis is −22°. The outer wall subunits are oriented in a plane perpendicular to the filament axis, while the inner wall subunits are tilted relative to the filament axis.

of the assembly (Fig. 6*C*). This axial tilt enabled lateral interactions between protofilaments that resulted in formation of the nanotube. In contrast, the protofilament tilt (∼22°) within the PSMβ2 nanotube was about half the value of that observed for the PSMα3 tubes (Fig. 6*D*). Instead, the subunits at the interior interface adopted a different orientation from the subunits at the outer interface in order to accommodate the circumferential disparity between the inner and outer layers of the nanotube (Fig. 6*D*). The outward-facing structural motifs were oriented in a plane nearly perpendicular to the helical axis of the nanotube, while the inward-facing structural motifs underwent a pronounced tilt with respect to the helical axis. This difference in orientation resulted in a crossing angle of ∼45° between PSMβ2 subunits across the mating interface between the inner and outer layers of the protofilaments (*SI Appendix*, Fig. S16). A key similarity shared by both PSMα3 and PSMβ2 nanotubes was that the vertical stacking distance between subunits in the outer wall was larger than the corresponding spacing in the inner wall. For the PSMα3 tubes, an 11.2- to 11.3-Å vertical stacking distance between adjacent outer wall subunits was present, while the same spacing in the inner wall was ∼10.9 Å for both diameters (Fig. 6*C*). For PSMβ2, the vertical spacing between identical residues between adjacent subunits on the same protofilament was ∼18 Å for both the outer and inner walls.

The results of the cryo-EM structural analysis clearly demonstrated that cross-α helical filaments can serve as components of higher-order peptide assemblies such as nanotubes. However, the relevance of the reported PSMα3 and PSMβ2 nanotubes to the pathophysiology of MRSA and other staphylococcal species is not immediately evident. PSMα3 is the most cytotoxic of the *S. aureus* PSM peptides (8) and has been demonstrated to have a strong propensity to self-assemble into different morphological variants based on cross-α protofilaments (22, 27, 29). The relationship of the PSMα3 assemblies to its cytotoxicity, as well as the identification of PSMs as functional bacterial amyloids, is a topic of current debate (21–23, 26, 27).

PSMβ2 also displays a strong potential for self-assembly and, as the current investigation demonstrates, for the formation of supramolecular structures derived from cross-α protofilaments. However, previously reported biochemical studies indicated that *S. aureus* PSMβ2 exhibits minimal cytotoxicity (8, 65). Therefore, the cross-α fold alone does not necessarily imply cellular cytotoxicity. While facially amphipathic character in a peptide sequence can underlie both membrane activity and self-assembly, the different behaviors do not perfectly coincide. Antimicrobial peptides often display conformational amphipathicity that enhances membrane activity but does not necessarily result in self-assembly into higher-order structures (18). Likewise, many peptide sequences have been designed to enhance facial amphipathicity in order to promote self-assembly, but in most cases the corresponding peptides do not exhibit antimicrobial activity. From this perspective, it is interesting to note that PSMβ peptides from other staphylococcal species, including close relatives of *S. aureus* PSMβ2 (66), have been reported to exhibit antimicrobial activity. In the latter case, the sequences of the PSMβ variants had undergone site-specific substitutions that might have enhanced amphipathic character vis-à-vis *S. aureus* PSMβ2. Knowledge of the *S. aureus* PSMβ2 structure provides the opportunity to better understand the role of such sequence variation on biological activity and self-assembly behavior.

The self-assembly behavior of *S. aureus* PSMα3 and PSMβ2 peptides provides strong supporting evidence for the importance

of the cross-α fold in self-assembled peptide and protein structures. While unrecognized prior to 2017, cross-α structures have been described at near-atomic resolution for a number of biologically derived or de novo designed peptides (22, 27, 61–63, 67, 68). The design space of the cross-α fold remains relatively unexplored, and the robustness of the fold in sequence space represents an open question that has recently begun to be addressed (63, 67). The supramolecular architecture of the cross-α fold appears superficially similar to the well-known cross-β fold (31, 69, 70), which forms the structural basis of amyloid fibrils (71) as well as many designed β-sheet peptides (15, 72–75). While the local peptide conformation and the nature of the cohesive interactions differ, cross-α and cross-β assemblies are both capable of forming bilayer protofilaments that interact through tightly packed mating interfaces (22).

In addition, as the results presented here suggest, structurally promiscuous self-assembly is observed for the PSM peptides, as has been often reported for the in vitro self-assembly of amyloidogenic peptides and proteins (76–79). The self-assembly of amyloidogenic peptides has been extensively explored in this regard, including with respect to the formation of nanotube assemblies (35–40). The results of our structural analyses of the PSMα3 and PSMβ2 peptide assemblies, in combination with previous results on designed helical peptides (61, 63), demonstrate that α-helical peptides undergo similar morphological transitions to those observed for the more thoroughly investigated cross-β assemblies. The relevance of the various assembled states to biological activity remains an open question, and it may be, as is frequently postulated for cross-β amyloids (80), that the filamentous forms represent a sequestered, inactive state of the peptide that may undergo gain of function after chemical or physical transformation into an active form. However, the polymorphism of the PSMα3 and PSMβ2 peptide assemblies provides evidence that the corresponding supramolecular structures can be dynamically remodeled in response to changes in environmental conditions. This dynamic response behavior may be critical for the biological activity of the PSM family of peptides. Structural transformations of PSMα3 have been observed to occur in the presence of cytomimetic membranes (26). These results suggest that it may not be possible to attribute cellular toxicity to a specific structure within the ensemble. Rather, the ability of the PSMα3 and PSMβ2 peptides to reversibly sample different structural states may be more relevant to their respective functions.

Finally, soft matter nanotubes (81, 82), particularly those derived from peptides and proteins, have attracted significant interest due to their potential use as biologically functional nanomaterials (83, 84). Structural transitions between polymorphs have been frequently exploited for the fabrication of novel nanomaterials from peptide assemblies (35, 48, 85, 86). However, the lability of helical symmetry in peptide design-space places a practical limit on ab initio structural prediction for helical filaments from sequence information alone and represents a significant challenge to the de novo design of peptide nanotubes and structurally related assemblies (34, 61, 87, 88). The availability of high-resolution structural information from cryo-EM analysis of biologically derived and designed protein filaments provides a reliable starting point for design efforts targeted toward developing functional filamentous nanomaterials. We recently demonstrated that computational design methods could be employed to optimize the properties (e.g., thermodynamic stability, solubility, and colloidal dispersibility) of a helical filament derived from a designed cross-α assembly without significant perturbation of its supramolecular structure (63). Since the structures of the PSMα3 and PSMβ2 nanotube assemblies have been determined at high resolution, the corresponding atomic models present the opportunity to explicitly design cross-α assemblies for potential applications as biologically active nanomaterials (e.g., as antimicrobial agents), as well as to interrogate the importance of specific amino acid residues within the native sequences for their effect on self-assembly and biological activity.

Materials and Methods

Peptide Synthesis. *N*-fluorenylmethyloxycarbonyl (Fmoc)–protected amino acids were purchased from AAPPTec, Inc. Fmoc-PAL-PEG-PS peptide synthesis resin was ordered from Life Technologies, Inc. All other chemical reagents were purchased from MilliporeSigma, Inc. PSMα3 was prepared via a microwave-assisted, solid-phase peptide synthesis on a CEM Liberty Blue instrument as the *N*-acetyl, *C*-amide capped derivative at a 0.1-mmol scale. Coupling reactions were conducted with 0.2 M Fmoc-protected amino acids in N,*N*-Dimethylformamide (DMF; activated with 0.5 M N,N'-Diisopropylcarbodiimide in DMF and 0.5 M ethyl cyanohydroxyiminoacetate (oxyma) in DMF. Peptides were cleaved from the resin by incubation at room temperature for 3 h in a 20-mL mixture consisting of 92.5% trifluoroacetic acid (TFA), 2.5% distilled water, 2.5% triisopropylsilane, and 2.5% 2,2'- (ethylenedioxy)-diethanethiol. The cleaved peptide solution was filtered and precipitated with 60 mL 4 °C diethyl ether, and the precipitate was allowed to desiccate overnight. Following desiccation, the crude peptide gels were resolubilized in 3 mL of a 50:50 mixture of acetonitrile and water (0.1% TFA) and purified by reversed-phase high-pressure liquid chromatography (HPLC). Peptide mass was confirmed using MALDI-TOF mass spectrometry on an Applied Biosystems AB4700 Proteomics analyzer in reflectron positive ion mode, with α-Cyano-4-hydroxycinnamic acid as the matrix. Purified HPLC fractions were then lyophilized, sealed, and stored at −30 °C. Peptides PSMα3 and PSMβ2 were also obtained from Synpeptide Co. Ltd. as the *N*-acetyl, C-amide derivative at ≥95% purity by analytical HPLC.

Peptide Assembly. Stock solutions of PSMα3 were prepared by solubilizing 0.5 to 1.5 mg purified, lyophilized peptide in HPLC water (1 mL). Stock solutions of peptide were diluted in a range of buffers to a final peptide concentration of 189 to 556 μM. Immediately after mixture, the solutions were titrated to the respective buffer pH using 100 mM sodium hydroxide solution. For the PSMα3 samples under acidic conditions, the stock solution was diluted to the appropriate concentration, and TFA was used to titrate to pH 2. Thermally annealed samples were prepared using the following protocol in a thermal cycler: 1) rapid heating to 90 °C for 30 min and 2) cooling to 25 °C at a rate of 0.2 °C/min. Stock solutions of PSMβ2 were prepared by solubilizing 0.5 mg purified, lyophilized peptide in 200 μL of the appropriate buffer, and the pH was adjusted to the appropriate value using titration with aqueous sodium hydroxide solution (100 mM). The samples were incubated at ambient temperature. For thermally annealed samples, the following protocol was employed in a thermal cycler: 1) rapid heating to 50/70/90 °C for 30 min and 2) cooling to 25 °C at a rate of 0.2 °C/min.

CD Spectropolarimetry. CD measurements were performed on a Jasco J-1500 CD spectropolarimeter using a 0.1-mm path length quartz cuvette from Hellma USA Inc. Three spectra were collected and averaged in a wavelength range from 190 to 260 nm at a scanning range of 100 nm/min with a bandwidth of 2 nm and a data pitch of 0.2 nm.

TEM. Grids were prepared using diluted aqueous solutions of peptide assemblies in which aliquots of sample (4 μL) were deposited onto a 200-mesh carbon-coated copper grid from Electron Microscopy Services. After 90 s of incubation on the grid, moisture was wicked away, leaving a thin film of sample. An aliquot (4 μL) of negative stain solution, either 1% uranyl acetate for PSMα3 or a 1:1 mixture of 1% methylamine tungstate (nano-W) and 1% methylamine vanadate (nanoVan) stains from Nanoprobes, Inc. for PSMβ2, was deposited onto the thin film. After 60 s of staining, the remaining moisture was wicked away, and the grid was dried in a tabletop desiccator in vacuo for at least 5 min. Electron micrographs were recorded on a Hitachi HT-7700 TEM with a tungsten filament and AMT CCD camera at an accelerating voltage of 80 kV.

STEM. STEM data were acquired at Brookhaven National Laboratory. The STEM instrument operates at 40 keV with a scanning probe of 0.3-nm diameter produced from a cold field-emission source. Specimens were deposited on thin carbon (ca. 2 nm thick) supported on a thicker holey carbon film mounted on a titanium grid using the wet-film, hanging-drop method. Tobacco mosaic virus (TMV) was added to the grid first as an internal control, followed by injection buffer, then specimen solution (in pH 2 water) for 1 min, and then 10 washes of 20 mM ammonium acetate, pH 7.0. Excess solution was wicked from the edge with filter paper between each injection. After the last wash, the grid was wicked to a thin layer (ca. 1 mm), fast frozen by plunging into liquid nitrogen slush, and stored under liquid nitrogen. Alternatively, grids were stained with 1% uranyl acetate, as described above, prior to image acquisition. Grids were freeze-dried overnight in an ion-pumped chamber with an efficient cold trap and transferred under vacuum to the STEM cold stage (−160 °C). Imaging typically uses a dose of 20 $e^{-}/Å^{2}$ (causing <5% mass loss, corrected by comparison to TMV).

Synchrotron SAXS/WAXS Measurements. Synchrotron SAXS/WAXS measurements were performed at the 12-ID-B beamline of the Advanced Photon Source at Argonne National Laboratory. A SAXS/WAXS simultaneous setup was utilized, and the sample-to-detector distances were set such that the overall scattering momentum transfer (q) range was achieved from 0.003 to 2.4 $Å^{-1}$, where $q = 4\pi\sin(\theta)/\lambda$, with 2θ denoting the scattering angle and λ denoting the X-ray wavelength. The wavelength was set at 0.9322 Å during the measurements. Scattered X-ray intensities were measured using a Pilatus 2 M (DECTRIS) detector for SAXS and Pilatus 300K for WAXS. SAXS/WAXS measurements were performed on aqueous solutions of the annealed PSMα3 peptide assemblies at a concentration of 4.0 mg/mL (ca. 3.4 mM) in water (pH 2.0) at 25 °C with addition of 1% glycerol to stabilize against X-ray beam damage. Prior to SAXS analysis, the peptide solutions were dialyzed against a large excess of water (1% glycerol, pH 2.0) for 24 h. A flow cell equipped with a quartz capillary (1.5-mm diameter) was used to prevent radiation damage. Twenty images were collected for each sample and buffer. The 2D scattering images were converted to one-dimensional (1D) SAXS curves through azimuthally averaging after solid angle correction and then normalizing with the intensity of the transmitted X-ray beam using the software package at beamline 12-ID-B. The 1D curves of the samples were averaged and subtracted with the background measured from the corresponding buffers. The simulated SAXS curves were calculated using the program CRYSOL (89) with fitting to a model based on the form factor for a hollow cylindrical particle, as previously described for aqueous solutions of cross-β nanotubes derived from self-assembly of the Aβ (16–22) peptide (35). The wall thickness was set to 30 Å as a known parameter, which was similar to the estimated hydrated thickness of a bilayer of PSMα3 based on crystallographic data. Length/height was set as 10,000 Å in order to get an approximately correct form factor for the high aspect-ratio nanotubes of PSMα3. Other parameters such as inner radius R2, background scattering intensity, and scaling factors were allowed to float in the data fitting.

Cryo-EM Sample Preparation and Data Collection. An aliquot (3 μL) of sample containing either PSMα3 or PSMβ2 assemblies was applied to a plasma-cleaned (Gatan Solarus) lacey carbon grid (Sigma-Aldrich), blotted with force of 3 to 6 for 4.0 s at 100% humidity, and flash frozen in liquid ethane using a Vitribot Mark IV (FEI). The datasets used for structure determination were collected at the National Cryo-Electron Microscopy Facility at the Frederick National Laboratory for Cancer Research on a Titan Krios EM operated at 300 keV, equipped with an energy filter and K3 direct electron detector (Gatan). An energy filter slit width of 20 eV was used during data collection and was aligned automatically every hour. A total of 18,751 (PSMα3) and 8,700 (PSMβ2) movies were collected in counting mode using EPU v2.4 (Thermo Fisher Scientific) at a magnification of 81K, a pixel size of 1.08 Å, and a defocus range from −2.2 to −1.2 μm. Data collection was performed using a total dose of 50 e^{-} $Å^{-2}$ across 40 frames with an exposure time of 2.98 s.

Cryo-EM Analysis and Helical Reconstruction. Movies were corrected for full-frame motion and dose using MotionCor (90). Contrast transfer function (CTF) correction was applied by multiplying the micrographs, corresponding to the first 20 frames with a total dose of ∼20 electrons/$Å^{2}$ with the theoretical CTF using CTFFIND3 (91). After CTF correction, filament images with discrete diameters of 370 Å (346 pixels) and 410 Å (376 pixels) were boxed manually and extracted using e2helixboxer (EMAN2) (92). The CTF-corrected micrographs were used for segment extraction box sizes of 420 and 400 pixels for the 370 Å and 410 Å PSMα3 tubes, respectively, and 384 pixels for the PSMβ2 tubes. For each filament, a list of possible helical symmetries was calculated from the averaged power spectrum of filament particles (*SI Appendix*, Fig. S17) (50). Subsequent processing and reconstruction was done using the SPIDER software (93). The correct helical symmetry was determined by trial and error until recognizable secondary structural and side chain densities were observed using IHRSR (51). In brief, the full dataset of each filament diameter underwent three steps where the helical symmetries were tightly locked in the first two steps and slightly relaxed in the third step. The helical symmetry parameters (rise, rotation, and point group symmetry) were imposed at the end of each IHRSR cycle. Once the correct helical symmetry was determined, the full dataset of particles was run in RELION (94) to generate a final reconstruction. The final resolutions achieved for the PSMα3 370 Å and 410 Å diameter tubes were 3.9 Å and 4.1 Å, respectively. The final resolution for the PSMβ2 nanotubes was 4.3 Å.

Model Building and Refinement. The density for each structure was enough to trace the entire backbone and localize most side chains. The previous PSMα3 crystal structure (PDB ID: 5I55) was used as a starting point for building the PSMα3 cryo-EM models. Following model completion, side chains of the models were manually adjusted in COOT (95) and analyzed in UCSF Chimera (96). The models were refined in PHENIX (97), using real-space refinement. Refinement included global minimization, B-factor optimization, and applied secondary structure and Ramachandran restraints. The final models were validated with the MolProbity (98) and the Ramachandran implementation in PHENIX. Refinement statistics for each filament diameter are listed in *SI Appendix*, Table S1. Both cryo-EM maps and atomic coordinates have been deposited with the Electron Microscopy Data Bank (EMDB) and PDB with the accession codes given in the *SI Appendix*, Table S1. Model-map correlation coefficients were employed to estimate the resolution of the reconstructions and are depicted in *SI Appendix*, Fig. S18 and reported in *SI Appendix*, Table S1. The cryo-EM and refinement statistics for each nanotube are listed in *SI Appendix*, Table S1.

Data Availability. Atomic coordinates have been deposited in the PDB with accession codes 7SZZ, 7T0X, and 7T8U. EM density maps have been deposited in the EMDB with accession codes EMD-25573, EMD-25584, and EMD-25747.

ACKNOWLEDGMENTS. Cryo-EM imaging of the PSMα3 and PSMβ2 filaments was performed at the Cryo-EM facility at the National Cancer Institute's Frederick Laboratory for Cancer Research under Contract No. HSSN261200800001E. This study was supported by the Robert P. Apkarian Integrated Electron Microscopy Core at Emory University, which is subsidized by the School of Medicine and Emory College of Arts and Sciences. Additional support was provided by the Georgia Clinical & Translational Science Alliance of the NIH under award number UL1TR000454. Negative-stain TEM images were gathered on a Hitachi HT7700 120kV TEM at Emory University, which was supported by the Georgia Clinical & Translational Science Alliance under award No. UL1TR002378. This research was supported by grants from the NSF (DMR-1534317) to V.P.C. and the NIH (GM122510) to E.H.E. The CD spectropolarimeter was acquired through funding from an NSF grant (DBI-1726544). M.A.B.K. acknowledges financial support from NIH T32 GM080186 and the University of Virginia Robert R. Wagner Fellowship. L.C.B. acknowledges financial support from NIH T32 AI007046. This research used resources of the Advanced Photon Source, a US Department of Energy (DOE) Office of Science User Facility, operated for the DOE Office of Science by Argonne National Laboratory under Contract No. DE-AC02-06CH11357. We thank Dr. Joseph Wall of Brookhaven National Laboratory for acquisition of the STEM imaging data.

Author affiliations: [a]Department of Biochemistry and Molecular Genetics, University of Virginia, Charlottesville, VA 22908; [b]Department of Chemistry, Emory University, Atlanta, GA 30322; [c]X-ray Science Division, Argonne National Laboratory, Lemont, IL 60439; and [d]The Robert P. Apkarian Integrated Electron Microscopy Core, Emory University, Atlanta, GA 30322

1. F. D. Lowy, Antimicrobial resistance: The example of *Staphylococcus aureus*. *J. Clin. Invest.* **111**, 1265–1273 (2003).
2. H. F. Chambers, F. R. Deleo, Waves of resistance: *Staphylococcus aureus* in the antibiotic era. *Nat. Rev. Microbiol.* **7**, 629–641 (2009).
3. F. R. DeLeo, M. Otto, B. N. Kreiswirth, H. F. Chambers, Community-associated meticillin-resistant *Staphylococcus aureus*. *Lancet* **375**, 1557–1568 (2010).
4. N. Tsouklidis, R. Kumar, S. E. Heindl, R. Soni, S. Khan, Understanding the fight against resistance: Hospital-acquired methicillin-resistant *Staphylococcus aureus* vs. community-acquired methicillin-resistant *Staphylococcus aureus*. *Cureus* **12**, e8867 (2020).
5. G. Y. Cheung, H. S. Joo, S. S. Chatterjee, M. Otto, Phenol-soluble modulins–Critical determinants of staphylococcal virulence. *FEMS Microbiol. Rev.* **38**, 698–719 (2014).
6. A. Peschel, M. Otto, Phenol-soluble modulins and staphylococcal infection. *Nat. Rev. Microbiol.* **11**, 667–673 (2013).
7. S. J. Klebanoff, D. H. Watts, C. Mehlin, C. M. Headley, Lactobacilli and vaginal host defense: Activation of the human immunodeficiency virus type 1 long terminal repeat, cytokine production, and NF-κB. *J. Infect. Dis.* **179**, 653–660 (1999).
8. R. Wang *et al.*, Identification of novel cytolytic peptides as key virulence determinants for community-associated MRSA. *Nat. Med.* **13**, 1510–1514 (2007).
9. D. Kretschmer *et al.*, Human formyl peptide receptor 2 senses highly pathogenic *Staphylococcus aureus*. *Cell Host Microbe* **7**, 463–473 (2010).
10. H. S. Joo, G. Y. Cheung, M. Otto, Antimicrobial activity of community-associated methicillin-resistant *Staphylococcus aureus* is caused by phenol-soluble modulin derivatives. *J. Biol. Chem.* **286**, 8933–8940 (2011).
11. M. Otto, Staphylococcal infections: Mechanisms of biofilm maturation and detachment as critical determinants of pathogenicity. *Annu. Rev. Med.* **64**, 175–188 (2013).
12. K. M. Towle *et al.*, Solution structures of phenol-soluble modulins α1, α3, and β2, virulence factors from *Staphylococcus aureus*. *Biochemistry* **55**, 4798–4806 (2016).
13. G. Y. Cheung *et al.*, Insight into structure-function relationship in phenol-soluble modulins using an alanine screen of the phenol-soluble modulin (PSM) α3 peptide. *FASEB J.* **28**, 153–161 (2014).
14. M. Laabei, W. D. Jamieson, Y. Yang, J. van den Elsen, A. T. Jenkins, Investigating the lytic activity and structural properties of *Staphylococcus aureus* phenol soluble modulin (PSM) peptide toxins. *Biochim. Biophys. Acta* **1838**, 3153–3161 (2014).
15. C. J. Bowerman, B. L. Nilsson, Self-assembly of amphipathic β-sheet peptides: Insights and applications. *Biopolymers* **98**, 169–184 (2012).
16. J. L. Beesley, D. N. Woolfson, The de novo design of α-helical peptides for supramolecular self-assembly. *Curr. Opin. Biotechnol.* **58**, 175–182 (2019).
17. S. Zhang, Discovery and design of self-assembling peptides. *Interface Focus* **7**, 20170028 (2017).
18. E. Y. Lee *et al.*, Functional reciprocity of amyloids and antimicrobial peptides: Rethinking the role of supramolecular assembly in host defense, immune activation, and inflammation. *Front. Immunol.* **11**, 1629 (2020).
19. B. L. Kagan, Antimicrobial amyloids? *Biophys. J.* **100**, 1597–1598 (2011).
20. B. L. Kagan *et al.*, Antimicrobial properties of amyloid peptides. *Mol. Pharm.* **9**, 708–717 (2012).
21. K. Schwartz, A. K. Syed, R. E. Stephenson, A. H. Rickard, B. R. Boles, Functional amyloids composed of phenol soluble modulins stabilize *Staphylococcus aureus* biofilms. *PLoS Pathog.* **8**, e1002744 (2012).
22. E. Tayeb-Fligelman *et al.*, The cytotoxic *Staphylococcus aureus* PSMα3 reveals a cross-α amyloid-like fibril. *Science* **355**, 831–833 (2017).
23. Y. Zheng, H. S. Joo, V. Nair, K. Y. Le, M. Otto, Do amyloid structures formed by *Staphylococcus aureus* phenol-soluble modulins have a biological function? *Int. J. Med. Microbiol.* **308**, 675–682 (2018).
24. N. Salinas, J. P. Colletier, A. Moshe, M. Landau, Extreme amyloid polymorphism in *Staphylococcus aureus* virulent PSMα peptides. *Nat. Commun.* **9**, 3512 (2018).
25. M. Zaman, M. Andreasen, Cross-talk between individual phenol-soluble modulins in *Staphylococcus aureus* biofilm enables rapid and efficient amyloid formation. *eLife* **9**, e59776 (2020).
26. R. Malishev *et al.*, Reciprocal interactions between membrane bilayers and *S. aureus* PSMα3 cross-α amyloid fibrils account for species-specific cytotoxicity. *J. Mol. Biol.* **430**, 1431–1441 (2018).
27. E. Tayeb-Fligelman, N. Salinas, O. Tabachnikov, M. Landau, *Staphylococcus aureus* PSMα3 cross-α fibril polymorphism and determinants of cytotoxicity. *Structure* **28**, 301–313.e6 (2020).
28. D. S. Eisenberg, M. R. Sawaya, Structural studies of amyloid proteins at the molecular level. *Annu. Rev. Biochem.* **86**, 69–95 (2017).
29. Z. Yao *et al.*, Use of a stereochemical strategy to probe the mechanism of phenol-soluble modulin α3 toxicity. *J. Am. Chem. Soc.* **141**, 7660–7664 (2019).
30. J.-P. Colletier *et al.*, Molecular basis for amyloid-β polymorphism. *Proc. Natl. Acad. Sci. U.S.A.* **108**, 16938–16943 (2011).
31. R. Diaz-Avalos *et al.*, Cross-beta order and diversity in nanocrystals of an amyloid-forming peptide. *J. Mol. Biol.* **330**, 1165–1175 (2003).
32. T. Eichner, S. E. Radford, A diversity of assembly mechanisms of a generic amyloid fold. *Mol. Cell* **43**, 8–18 (2011).
33. J. Adamcik, R. Mezzenga, Amyloid polymorphism in the protein folding and aggregation energy landscape. *Angew. Chem. Int. Ed. Engl.* **57**, 8370–8382 (2018).
34. F. Wang *et al.*, Deterministic chaos in the self-assembly of β sheet nanotubes from an amphipathic oligopeptide. *Matter* **4**, 3217–3231 (2021).
35. K. Lu, J. Jacob, P. Thiyagarajan, V. P. Conticello, D. G. Lynn, Exploiting amyloid fibril lamination for nanotube self-assembly. *J. Am. Chem. Soc.* **125**, 6391–6393 (2003).
36. J. Adamcik, V. Castelletto, S. Bolisetty, I. W. Hamley, R. Mezzenga, Direct observation of time-resolved polymorphic states in the self-assembly of end-capped heptapeptides. *Angew. Chem. Int. Ed. Engl.* **50**, 5495–5498 (2011).
37. K. L. Morris *et al.*, The structure of cross-β tapes and tubes formed by an octapeptide, αSβ1. *Angew. Chem. Int. Ed. Engl.* **52**, 2279–2283 (2013).
38. Y. Zhao *et al.*, Tuning the self-assembly of short peptides via sequence variations. *Langmuir* **29**, 13457–13464 (2013).
39. Y. Zhao, L. Deng, J. Wang, H. Xu, J. R. Lu, Solvent controlled structural transition of KI4K self-assemblies: From nanotubes to nanofibrils. *Langmuir* **31**, 12975–12983 (2015).
40. Y. Zhao *et al.*, Controlling the diameters of nanotubes self-assembled from designed peptide bolaphiles. *Small* **14**, e1703216 (2018).
41. R. Ghafouri, R. Bruinsma, Helicoid to spiral ribbon transition. *Phys. Rev. Lett.* **94**, 138101 (2005).
42. I. Usov, J. Adamcik, R. Mezzenga, Polymorphism complexity and handedness inversion in serum albumin amyloid fibrils. *ACS Nano* **7**, 10465–10474 (2013).
43. I. Usov, R. Mezzenga, Correlation between nanomechanics and polymorphic conformations in amyloid fibrils. *ACS Nano* **8**, 11035–11041 (2014).
44. R. L. Selinger, J. V. Selinger, A. P. Malanoski, J. M. Schnur, Shape selection in chiral self-assembly. *Phys. Rev. Lett.* **93**, 158103 (2004).
45. R. L. Selinger, J. V. Selinger, A. P. Malanoski, J. M. Schnur, Visualizing chiral self-assembly. *Chaos* **14**, S3 (2004).
46. Y. Sawa *et al.*, Shape selection of twist-nematic-elastomer ribbons. *Proc. Natl. Acad. Sci. U.S.A.* **108**, 6364–6368 (2011).
47. T. R. Pearce, E. Kokkoli, DNA nanotubes and helical nanotapes via self-assembly of ssDNA-amphiphiles. *Soft Matter* **11**, 109–117 (2015).
48. L. Ziserman, H. Y. Lee, S. R. Raghavan, A. Mor, D. Danino, Unraveling the mechanism of nanotube formation by chiral self-assembly of amphiphiles. *J. Am. Chem. Soc.* **133**, 2511–2517 (2011).
49. L. Ziserman, A. Mor, D. Harries, D. Danino, Curvature instability in a chiral amphiphile self-assembly. *Phys. Rev. Lett.* **106**, 238105 (2011).
50. F. Wang, O. Gnewou, A. Solemanifar, V. P. Conticello, E. H. Egelman, Cryo-EM of helical polymers. *Chem. Rev.*, 10.1021/acs.chemrev.1c00753 (2022).
51. E. H. Egelman, A robust algorithm for the reconstruction of helical filaments using single-particle methods. *Ultramicroscopy* **85**, 225–234 (2000).
52. E. H. Egelman, The iterative helical real space reconstruction method: Surmounting the problems posed by real polymers. *J. Struct. Biol.* **157**, 83–94 (2007).
53. S. De Carlo, J. R. Harris, Negative staining and cryo-negative staining of macromolecules and viruses for TEM. *Micron* **42**, 117–131 (2011).
54. D. Chrétien, F. Metoz, F. Verde, E. Karsenti, R. H. Wade, Lattice defects in microtubules: Protofilament numbers vary within individual microtubules. *J. Cell Biol.* **117**, 1031–1040 (1992).
55. S. Chaaban, G. J. Brouhard, A microtubule bestiary: Structural diversity in tubulin polymers. *Mol. Biol. Cell* **28**, 2924–2931 (2017).
56. J. L. Jiménez *et al.*, The protofilament structure of insulin amyloid fibrils. *Proc. Natl. Acad. Sci. U.S.A.* **99**, 9196–9201 (2002).
57. J. D. Brodin, S. J. Smith, J. R. Carr, F. A. Tezcan, Designed, helical protein nanotubes with variable diameters from a single building block. *J. Am. Chem. Soc.* **137**, 10468–10471 (2015).
58. Z. Feng *et al.*, Artificial intracellular filaments. *Cell Rep. Phys. Sci.* **1**, 100085 (2020).
59. M. Baek *et al.*, Accurate prediction of protein structures and interactions using a three-track neural network. *Science* **373**, 871–876 (2021).
60. S. A. Hughes *et al.*, Ambidextrous helical nanotubes from self-assembly of designed helical hairpin motifs. *Proc. Natl. Acad. Sci. U.S.A.* **116**, 14456–14464 (2019).
61. E. H. Egelman *et al.*, Structural plasticity of helical nanotubes based on coiled-coil assemblies. *Structure* **23**, 280–289 (2015).
62. F. DiMaio *et al.*, Atomic-accuracy models from 4.5-Å cryo-electron microscopy data with density-guided iterative local refinement. *Nat. Methods* **12**, 361–365 (2015).
63. F. Wang *et al.*, Structural analysis of cross α-helical nanotubes provides insight into the designability of filamentous peptide nanomaterials. *Nat. Commun.* **12**, 407 (2021).
64. E. Krissinel, K. Henrick, Inference of macromolecular assemblies from crystalline state. *J. Mol. Biol.* **372**, 774–797 (2007).
65. G. Y. Cheung, A. C. Duong, M. Otto, Direct and synergistic hemolysis caused by *Staphylococcus* phenol-soluble modulins: Implications for diagnosis and pathogenesis. *Microbes Infect.* **14**, 380–386 (2012).
66. R. Kumar, P. K. Jangir, J. Das, B. Taneja, R. Sharma, Genome analysis of *Staphylococcus capitis* TE8 reveals repertoire of antimicrobial peptides and adaptation strategies for growth on human skin. *Sci. Rep.* **7**, 10447 (2017).
67. S. Q. Zhang *et al.*, Designed peptides that assemble into cross-α amyloid-like structures. *Nat. Chem. Biol.* **14**, 870–875 (2018).
68. N. Salinas *et al.*, The amphibian antimicrobial peptide uperin 3.5 is a cross-α/cross-β chameleon functional amyloid. *Proc. Natl. Acad. Sci. U.S.A.* **118**, e2014442118 (2021).
69. E. D. Eanes, G. G. Glenner, X-ray diffraction studies on amyloid filaments. *J. Histochem. Cytochem.* **16**, 673–677 (1968).
70. M. Sunde *et al.*, Common core structure of amyloid fibrils by synchrotron X-ray diffraction. *J. Mol. Biol.* **273**, 729–739 (1997).
71. P. C. Ke *et al.*, Half a century of amyloids: Past, present and future. *Chem. Soc. Rev.* **49**, 5473–5509 (2020).
72. S. Zhang, T. Holmes, C. Lockshin, A. Rich, Spontaneous assembly of a self-complementary oligopeptide to form a stable macroscopic membrane. *Proc. Natl. Acad. Sci. U.S.A.* **90**, 3334–3338 (1993).
73. D. M. Marini, W. Hwang, D. A. Lauffenburger, S. Zhang, R. D. Kamm, Left-handed helical ribbon intermediates in the self-assembly of a β-sheet peptide. *Nano Lett.* **2**, 295–299 (2002).
74. A. Aggeli *et al.*, Responsive gels formed by the spontaneous self-assembly of peptides into polymeric β-sheet tapes. *Nature* **386**, 259–262 (1997).
75. J. P. Schneider *et al.*, Responsive hydrogels from the intramolecular folding and self-assembly of a designed peptide. *J. Am. Chem. Soc.* **124**, 15030–15037 (2002).
76. W. Close *et al.*, Physical basis of amyloid fibril polymorphism. *Nat. Commun.* **9**, 699 (2018).
77. M. Kollmer *et al.*, Cryo-EM structure and polymorphism of Aβ amyloid fibrils purified from Alzheimer's brain tissue. *Nat. Commun.* **10**, 4760 (2019).
78. W. Zhang *et al.*, Heparin-induced tau filaments are polymorphic and differ from those in Alzheimer's and Pick's diseases. *eLife* **8**, e43584 (2019).
79. E. L. Guenther *et al.*, Atomic-level evidence for packing and positional amyloid polymorphism by segment from TDP-43 RRM2. *Nat. Struct. Mol. Biol.* **25**, 311–319 (2018).
80. M. Stefani, Structural features and cytotoxicity of amyloid oligomers: Implications in Alzheimer's disease and other diseases with amyloid deposits. *Prog. Neurobiol.* **99**, 226–245 (2012).
81. T. Shimizu, W. Ding, N. Kameta, Soft-matter nanotubes: A platform for diverse functions and applications. *Chem. Rev.* **120**, 2347–2407 (2020).
82. I. W. Hamley, Peptide nanotubes. *Angew. Chem. Int. Ed. Engl.* **53**, 6866–6881 (2014).
83. Y. Wu *et al.*, A supramolecular vaccine platform based on α-helical peptide nanofibers. *ACS Biomater. Sci. Eng.* **3**, 3128–3132 (2017).

84. C. N. Fries *et al.*, Controlled lengthwise assembly of helical peptide nanofibers to modulate $CD8^+$ T-cell responses. *Adv. Mater.* **32**, e2003310 (2020).
85. Y. Tian *et al.*, Nanotubes, plates, and needles: Pathway-dependent self-assembly of computationally designed peptides. *Biomacromolecules* **19**, 4286–4298 (2018).
86. A. D. Merg *et al.*, Shape-shifting peptide nanomaterials: Surface asymmetry enables pH-dependent formation and interconversion of collagen tubes and sheets. *J. Am. Chem. Soc.* **142**, 19956–19968 (2020).
87. A. Lu *et al.*, Plasticity in PYD assembly revealed by cryo-EM structure of the PYD filament of AIM_2. *Cell Discov.* **1**, 15013 (2015).
88. V. E. Galkin, A. Orlova, G. F. Schröder, E. H. Egelman, Structural polymorphism in F-actin. *Nat. Struct. Mol. Biol.* **17**, 1318–1323 (2010).
89. D. Svergun, C. Barberato, M. H. J. Koch, CRYSOL– A program to evaluate X-ray solution scattering of biological macromolecules from atomic coordinates. *J. Appl. Cryst.* **28**, 768–773 (1995).
90. S. Q. Zheng *et al.*, MotionCor2: Anisotropic correction of beam-induced motion for improved cryo-electron microscopy. *Nat. Methods* **14**, 331–332 (2017).
91. J. A. Mindell, N. Grigorieff, Accurate determination of local defocus and specimen tilt in electron microscopy. *J. Struct. Biol.* **142**, 334–347 (2003).
92. G. Tang *et al.*, EMAN2: An extensible image processing suite for electron microscopy. *J. Struct. Biol.* **157**, 38–46 (2007).
93. J. Frank *et al.*, SPIDER and WEB: Processing and visualization of images in 3D electron microscopy and related fields. *J. Struct. Biol.* **116**, 190–199 (1996).
94. S. H. W. Scheres, RELION: Implementation of a Bayesian approach to cryo-EM structure determination. *J. Struct. Biol.* **180**, 519–530 (2012).
95. P. Emsley, B. Lohkamp, W. G. Scott, K. Cowtan, Features and development of Coot. *Acta Crystallogr. D Biol. Crystallogr.* **66**, 486–501 (2010).
96. E. F. Pettersen *et al.*, UCSF Chimera–A visualization system for exploratory research and analysis. *J. Comput. Chem.* **25**, 1605–1612 (2004).
97. P. D. Adams *et al.*, PHENIX: A comprehensive Python-based system for macromolecular structure solution. *Acta Crystallogr. D Biol. Crystallogr.* **66**, 213–221 (2010).
98. C. J. Williams *et al.*, MolProbity: More and better reference data for improved all-atom structure validation. *Protein Sci.* **27**, 293–315 (2018).